

# Electric field metrology for SI traceability: Systematic measurement uncertainties in electromagnetically induced transparency in atomic vapor

Christopher L. Holloway, Matt T. Simons, Joshua A. Gordon, Andrew Dienstfrey, David A. Anderson, and Georg Raithel

Citation: *Journal of Applied Physics* **121**, 233106 (2017); doi: 10.1063/1.4984201

View online: <http://dx.doi.org/10.1063/1.4984201>

View Table of Contents: <http://aip.scitation.org/toc/jap/121/23>

Published by the *American Institute of Physics*

---

---

**AIP** | Journal of  
Applied Physics

Save your money for your research.  
It's now **FREE** to publish with us -  
no page, color or publication charges apply.

Publish your research in the  
*Journal of Applied Physics*  
to claim your place in applied  
physics history.

# Electric field metrology for SI traceability: Systematic measurement uncertainties in electromagnetically induced transparency in atomic vapor

Christopher L. Holloway,<sup>1,a)</sup> Matt T. Simons,<sup>1</sup> Joshua A. Gordon,<sup>1</sup> Andrew Dienstfrey,<sup>1</sup> David A. Anderson,<sup>2</sup> and Georg Raithel<sup>2,3</sup>

<sup>1</sup>National Institute of Standards and Technology (NIST), Boulder, Colorado 80305, USA

<sup>2</sup>Rydberg Technologies, LLC, Ann Arbor, Michigan 48109, USA

<sup>3</sup>Department of Physics, University of Michigan, Ann Arbor, Michigan 48109, USA

(Received 4 April 2017; accepted 14 May 2017; published online 20 June 2017)

We investigate the relationship between the Rabi frequency ( $\Omega_{RF}$ , related to the applied electric field) and Autler-Townes (AT) splitting, when performing atom-based radio-frequency (RF) electric (E) field strength measurements using Rydberg states and electromagnetically induced transparency (EIT) in an atomic vapor. The AT splitting satisfies, under certain conditions, a well-defined linear relationship with the applied RF field amplitude. The EIT/AT-based E-field measurement approach derived from these principles is currently being investigated by several groups around the world as a means to develop a new SI-traceable RF E-field measurement technique. We establish conditions under which the measured AT-splitting is an approximately linear function of the RF electric field. A quantitative description of systematic deviations from the linear relationship is key to exploiting EIT/AT-based atomic-vapor spectroscopy for SI-traceable field measurement. We show that the linear relationship is valid and can be used to determine the E-field strength, with minimal error, as long as the EIT linewidth is small compared to the AT-splitting. We also discuss interesting aspects of the thermal dependence (i.e., hot- versus cold-atom) of this EIT-AT technique. An analysis of the transition from cold- to hot-atom EIT in a Doppler-mismatched cascade system reveals a significant change of the dependence of the EIT linewidth on the optical Rabi frequencies and of the AT-splitting on  $\Omega_{RF}$ . [<http://dx.doi.org/10.1063/1.4984201>]

## I. INTRODUCTION

Recently, there has been an interest in the development of a novel spectroscopic approach for electric (E) field measurements<sup>1–9</sup> that can lead to a direct International System of Units (SI) traceable, self-calibrated measurement, that has the capability to perform measurements on a fine spatial resolution. The approach utilizes the phenomena of electromagnetically induced transparency (EIT) and Autler-Townes (AT) splitting.<sup>1–3,10</sup> This technique has the capability of becoming a new international standard for E-field measurements and calibrations. For a new measurement method to be accepted by National Metrology Institutes, including the National Institute of Standards and Technology (NIST), the accuracy and uncertainties of the approach must be assessed. Knowing the uncertainties of a technique is an important step when establishing a new international measurement standard for an E-field strength and is a necessary step for this method to be accepted as a standard calibration technique. Here, we look at one aspect of the measurement uncertainties/errors of this E-field measurement approach. We further investigate the effects of the atom temperature on the radio frequency (RF) E-field measurement by investigating the transitional behavior of EIT spectra from the cold-atom ( $T = 1 \mu\text{K}$ ) to the hot-atom ( $T = 300 \text{K}$ ) case. Our analysis sheds light on several important aspects, including the emergence of the Doppler correction factor in hot-atom,

vapor-cell EIT, and a change in the dependence of EIT linewidth on the optical Rabi frequencies.

This measurement approach can be represented by the four-level atomic system shown in Fig. 1. In effect, the “probe” laser is used to probe the response of the ground-state transition of the atoms, and a second laser (“coupling” laser) is used to excite the atoms to a high energy state. In the presence of the coupling laser, a destructive quantum

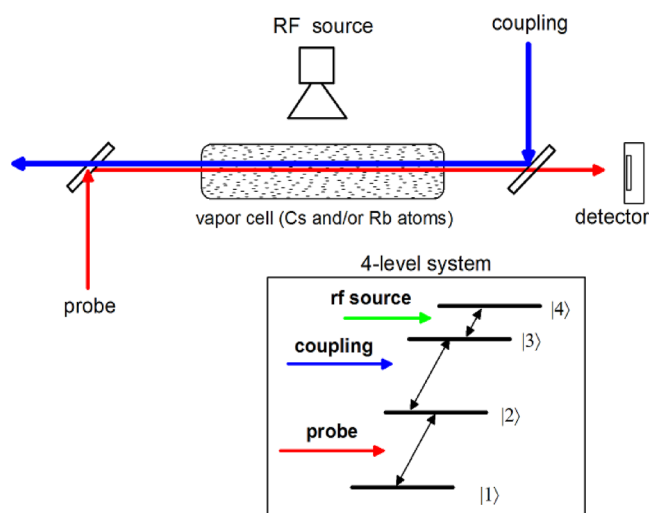


FIG. 1. Illustration of a four-level system and the vapor cell setup for measuring EIT, with counter-propagating probe and coupling beams. The RF field propagates transversely to the optical beams in the vapor cell.

<sup>a)</sup>holloway@boulder.nist.gov

interference occurs and the atoms become transparent to the resonant probe laser (this is the concept of EIT). A transparency window is opened for the probe laser light: probe light transmission is increased. The coupling laser wavelength is chosen such that the atom is in a sufficiently high state (a Rydberg state) such that a radio frequency (RF) field couples two Rydberg states (levels 3 and 4 in Fig. 1). The RF field in the four-level atomic system causes constructive interference of excitation pathways within the EIT transmission window, resulting in a decreased transmission of the probe laser and splitting (AT splitting) of the EIT peak. A typical measured spectrum with and without an RF source is shown in Fig. 2. In this figure,  $\Delta_p$  is the detuning of the probe laser from the ground state transition of the atom (where  $\Delta_p = \omega_p - \omega_o$ ;  $\omega_o$  is the on-resonance angular frequency of the ground state transition and  $\omega_p$  is the angular frequency of the probe laser).

The AT splitting (defined as  $2\pi\Delta f_o$ ) of the probe laser spectrum is easily measured and under certain conditions is equal to the Rabi frequency of the RF transition, or

$$\text{AT splitting} = 2\pi\Delta f_o = \Omega_{RF}, \quad (1)$$

where  $\Omega_{RF} = |E|\varphi/\hbar$  is the Rabi frequency of the RF transition,  $\hbar$  is Planck's constant, and  $\varphi$  is the dipole moment of the RF atomic transition. This relationship between the AT splitting and the Rabi frequency is obtained under the weak probe limit and for no Doppler averaging. By measuring this splitting ( $\Delta f_m$ ), we get a direct measurement of the RF E-field strength. In this approach, either the probe or the coupling laser can be scanned or detuned. For either case, the E-field strength is given by Refs. 2 and 3

$$|E| = 2\pi\frac{\hbar}{\varphi}D\Delta f_m = 2\pi\frac{\hbar}{\varphi}\Delta f_o, \quad (2)$$

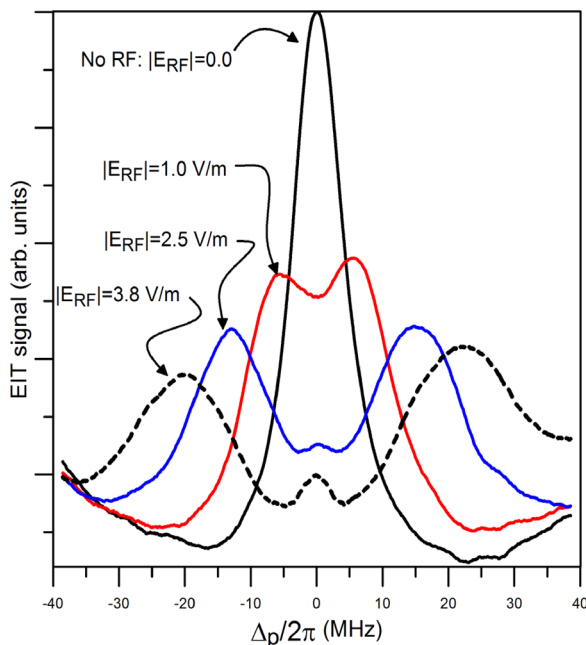


FIG. 2. Experimental data for the EIT signal (i.e., probe laser transmission through the cell) as a function of probe laser detuning  $\Delta p$ . This dataset is for a RF of 15.095 GHz and corresponds to the following  $^{85}\text{Rb}$  4-level atomic system:  $5S_{1/2} - 5P_{3/2} - 5D_{5/2} - 53P_{3/2}$ .

where  $\Delta f_m$  is the measured splitting,  $\Delta f_o = D\Delta f_m$ , and  $D$  is a parameter whose value depends on which of the two lasers is scanned during the measurement. If the probe laser is scanned,  $D = \frac{\lambda_p}{\lambda_c}$ ;  $\lambda_p$  and  $\lambda_c$  are the wavelengths of the probe and coupling laser, respectively. The  $\lambda_p/\lambda_c$  ratio is needed to account for the Doppler mismatch of the probe and coupling lasers<sup>10</sup> when the probe laser is scanned. If the coupling laser is scanned, it is not required to correct for the Doppler mismatch, and as a result  $D = 1$ . We consider this type of measurement of the E-field strength a direct SI-traceable, self-calibrated measurement in that it is related to Planck's constant (which will become an SI-defined quantity by standard bodies in the near future) and only requires a frequency measurement ( $\Delta f_m$ , which can be measured very accurately). The atomic dipole moment  $\varphi$  is a parameter which can be calculated accurately.<sup>2,11</sup>

Various aspects of the uncertainties of this type of measurement are currently being investigated.<sup>1-3,7,14,15</sup> In this paper, we investigate the validity of Eq. (2) and determine conditions when it is valid. Under certain conditions, the linear relationship between  $\Delta f_o$  and  $|E|$  as predicted from Eq. (2) can break down and the relationship becomes non-linear and, hence, calls into question the validity of Eq. (2). One such case is shown in Fig. 3, where we plot  $\Delta f_o$  versus  $|E|$ . (The quantity " $\sqrt{W}$ " on the x-axis is proportional to the applied RF E-field, where  $W$  represents the RF generator power.) The results in Fig. 3 are for measurements performed in  $^{133}\text{Cs}$  at 10.7 GHz. We see that when  $|E|$  is small (or for small  $\Delta f_o$ ), the data exhibit a nonlinear behavior. Linearity only applies for large values of  $|E|$ ; i.e., the linear relationship fails for small  $|E|$ . This same nonlinear behavior has been observed by others.<sup>16-18</sup> The expected linear behavior predicted in Eq. (2) is based on the assumption that the AT splitting of the EIT signal is proportional to the RF Rabi frequency

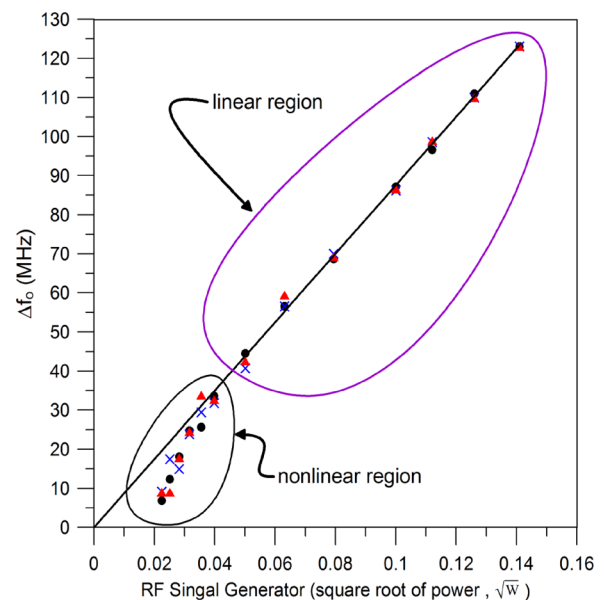


FIG. 3. Example of non-linear behavior. This dataset is for a RF of 10.7 GHz and corresponds to the following  $^{133}\text{Cs}$  4-level atomic system:  $6S_{1/2} - 6P_{3/2} - 41D_{5/2} - 42P_{3/2}$ . The three different symbols correspond to three different datasets. The numbers (square root of power, i.e.,  $\sqrt{W}$ ) stated on the x-axis are the values from the signal generator (SG) that feeds the waveguide which, in turn, feeds the horn antenna. As such, the quantity " $\sqrt{W}$ " on the x-axis is proportional to the applied RF E-field.

( $\Omega_{RF}$ ). The validity of Eq. (2) is a key aspect of the uncertainty of this measurement approach. When the data in the non-linear region are used with Eq. (2), then the E-field would be either underestimated or overestimated. The reason this non-linear behavior is observed is due to the linewidth of the EIT signal. If the EIT linewidth is comparable to or larger than  $\Delta f_o$ , then the linear relationship fails. In most of these cases, including the non-linear regime in Fig. 3, the AT splitting is artificially pulled closer together for simultaneously large EIT linewidths and small E-field values (or small  $\Delta f_o$ ). We investigate these effects by performing numerical studies of the four-level EIT signal for a range of conditions. We also explore how the temperature of the atomic vapor affects the linewidth of the EIT signal and thus the range of the non-linear behavior. We note that the splitting observed in the case of off-resonant AT effect is intrinsically non-linear,<sup>19</sup> in the present work, we focus on non-linear AT splittings observed in the case of on-resonant AT effect.

## II. FOUR-LEVEL EIT MODEL

In the model and the results presented in the following, we use parameters for <sup>85</sup>Rb as a typical, specific example. Similar results apply to other typical cases, such as <sup>87</sup>Rb (which merely differs in partial vapor pressure) and <sup>133</sup>Cs. We start by noting that the power of the probe beam measured on the detector (the EIT signal, i.e., the probe transmission through the vapor cell) is given by<sup>13</sup>

$$P = P_0 \exp\left(-\frac{2\pi L \text{Im}[\chi]}{\lambda_p}\right) = P_0 \exp(-\alpha L), \quad (3)$$

where  $P_0$  is the power of the probe beam at the input of the cell,  $L$  is the length of the cell,  $\lambda_p$  is the wavelength of the probe laser,  $\chi$  is the susceptibility of the medium seen by the probe laser, and  $\alpha = 2\pi \text{Im}[\chi]/\lambda_p$  is the Beer's absorption coefficient for the probe laser. The susceptibility for the probe laser is related to the density matrix component ( $\rho_{21}$ ) that is associated with the  $|1\rangle$ - $|2\rangle$  transition by the following:<sup>13</sup>

$$\chi = \frac{2\mathcal{N}_0 \wp_{12}}{E_p \epsilon_0} \rho_{21D}, \quad (4)$$

where the subscript  $D$  on  $\rho_{12}$  presents a Doppler averaged value,  $\mathcal{N}_0$  is the total density of atoms in the cell and is given by

$$\mathcal{N}_0 = 0.7217 \frac{p}{k_B T}, \quad (5)$$

where  $k_B$  is the Boltzmann constant,  $T$  is the temperature in Kelvin, and the pressure  $p$  (in units of Pa) is given by<sup>12</sup>

$$p = 10^{5.006 + 4.857 - \frac{4215}{T}}. \quad (6)$$

The factor 0.7217 in Eq. (5) reflects the natural abundance of <sup>85</sup>Rb. Note that this density is for vapor above solid Rb. A different expression applies for vapor above liquid Rb.<sup>12</sup> In Eq. (4),  $\wp_{12}$  is the dipole moment for the  $|1\rangle$ - $|2\rangle$  transition,  $\epsilon_0$  is the vacuum permittivity, and  $E_p$  is the amplitude of the probe laser E-field.

The density matrix component ( $\rho_{21}$ ) is obtained from the master equation<sup>13</sup>

$$\dot{\rho} = \frac{\partial \rho}{\partial t} = -\frac{i}{\hbar}[H, \rho] + \mathcal{L}, \quad (7)$$

where  $H$  is the Hamiltonian of the atomic system under consideration and  $\mathcal{L}$  is the Lindblad operator that accounts for the decay processes in the atom.

For the four level system, the Hamiltonian can be expressed as

$$H = \frac{\hbar}{2} \begin{bmatrix} 0 & \Omega_p & 0 & 0 \\ \Omega_p & -2\Delta_p & \Omega_c & 0 \\ 0 & \Omega_c & -2(\Delta_p + \Delta_c) & \Omega_{RF} \\ 0 & 0 & \Omega_{RF} & -2(\Delta_p + \Delta_c + \Delta_{RF}) \end{bmatrix}, \quad (8)$$

where  $\Delta_p$ ,  $\Delta_c$ , and  $\Delta_{RF}$  are the detunings of the probe laser, couple laser, and the RF source, respectively; and  $\Omega_p$ ,  $\Omega_c$ , and  $\Omega_{RF}$  are the Rabi frequencies associated with the probe laser, coupling laser, and the RF field, respectively. The detuning for each field is defined as

$$\Delta_{p,c,RF} = \omega_{p,c,RF} - \omega_{o_{p,c,RF}}, \quad (9)$$

where  $\omega_{o_{p,c,RF}}$  are the on-resonance angular frequencies of transitions  $|1\rangle$ - $|2\rangle$ ,  $|2\rangle$ - $|3\rangle$ , and  $|3\rangle$ - $|4\rangle$ , respectively; and  $\omega_{p,c,RF}$  are the angular frequencies of the probe laser, coupling laser, and the RF source, respectively. The Rabi frequencies are defined as  $\Omega_{p,c,RF} = |E_{p,c,RF}| \frac{\wp_{p,c,RF}}{\hbar}$ , where  $|E_{p,c,RF}|$  are the magnitudes of the E-field of the probe laser, the coupling laser, and the RF source, respectively. Finally,  $\wp_p$ ,  $\wp_c$ , and  $\wp_{RF}$  are the atomic dipole moments corresponding to the probe, coupling, and RF transitions, respectively.

For the four-level system, the  $\mathcal{L}$  matrix is given by

$$\mathcal{L} = \begin{bmatrix} \Gamma_2 \rho_{22} & -\gamma_{12} \rho_{12} & -\gamma_{13} \rho_{13} & -\gamma_{14} \rho_{14} \\ -\gamma_{21} \rho_{21} & \Gamma_3 \rho_{33} - \Gamma_2 \rho_{22} & -\gamma_{23} \rho_{23} & -\gamma_{24} \rho_{24} \\ -\gamma_{31} \rho_{31} & -\gamma_{32} \rho_{32} & \Gamma_4 \rho_{44} - \Gamma_3 \rho_{33} & -\gamma_{34} \rho_{34} \\ -\gamma_{41} \rho_{41} & -\gamma_{42} \rho_{42} & -\gamma_{43} \rho_{43} & -\Gamma_4 \rho_{44} \end{bmatrix}, \quad (10)$$

where  $\gamma_{ij} = (\Gamma_i + \Gamma_j)/2$  and  $\Gamma_{ij}$  are the transition decay rates. Since the purpose of the present study is to explore the intrinsic limitations of Rydberg-EIT field sensing in vapor cells, no collision terms or dephasing terms are added. While Rydberg-atom collisions, Penning ionization, and ion electric fields can, in principle, cause dephasing, such effects can, for instance, be alleviated by reducing the beam intensities, lowering the vapor pressure, or limiting the atom-field interaction time. In this analysis, we set  $\Gamma_1 = 0$ ,  $\Gamma_2 = 2\pi \times (6 \text{ MHz})$ ,  $\Gamma_3 = 2\pi \times (3 \text{ kHz})$ , and  $\Gamma_4 = 2\pi \times (2 \text{ kHz})$ .  $\Gamma_2$  is for the D2 line in <sup>85</sup>Rb,<sup>12</sup> and  $\Gamma_3$  and  $\Gamma_4$  are typical Rydberg decay rates.

Substituting  $H$  and  $\mathcal{L}$  into Eq. (7), the diagonal density matrix components are given by

$$\begin{aligned}
\dot{\rho}_{11} &= i\frac{\Omega_p}{2}(\rho_{12} - \rho_{21}) + \Gamma_2\rho_{22} \\
\dot{\rho}_{22} &= -i\frac{\Omega_p}{2}(\rho_{12} - \rho_{21}) + i\frac{\Omega_c}{2}(\rho_{23} - \rho_{32}) - \Gamma_2\rho_{22} + \Gamma_3\rho_{33} \\
\dot{\rho}_{33} &= -i\frac{\Omega_c}{2}(\rho_{23} - \rho_{32}) + i\frac{\Omega_{RF}}{2}(\rho_{34} - \rho_{43}) - \Gamma_3\rho_{33} + \Gamma_4\rho_{44} \\
\dot{\rho}_{44} &= -i\frac{\Omega_{RF}}{2}(\rho_{34} - \rho_{43}) - \Gamma_4\rho_{44}
\end{aligned} \tag{11}$$

and the off-diagonal density matrix components are given by

$$\begin{aligned}
\dot{\rho}_{21} &= [i\Delta_p - \gamma_{21}]\rho_{21} + i\frac{\Omega_p}{2}(\rho_{22} - \rho_{11}) - i\frac{\Omega_c}{2}\rho_{31} \\
\dot{\rho}_{31} &= [i(\Delta_p + \Delta_c) - \gamma_{31}]\rho_{31} + i\frac{\Omega_p}{2}\rho_{32} - i\frac{\Omega_c}{2}\rho_{21} - i\frac{\Omega_{RF}}{2}\rho_{41} \\
\dot{\rho}_{41} &= [i(\Delta_p + \Delta_c + \Delta_{RF}) - \gamma_{41}]\rho_{41} + i\frac{\Omega_p}{2}\rho_{42} - i\frac{\Omega_{RF}}{2}\rho_{31} \\
\dot{\rho}_{32} &= [i\Delta_c - \gamma_{32}]\rho_{32} + i\frac{\Omega_c}{2}(\rho_{33} - \rho_{22}) + i\frac{\Omega_p}{2}\rho_{31} - i\frac{\Omega_{RF}}{2}\rho_{42} \\
\dot{\rho}_{42} &= [i(\Delta_c + \Delta_{RF}) - \gamma_{42}]\rho_{42} + i\frac{\Omega_p}{2}\rho_{41} + i\frac{\Omega_c}{2}\rho_{43} - i\frac{\Omega_{RF}}{2}\rho_{32} \\
\dot{\rho}_{43} &= [i\Delta_{RF} - \gamma_{43}]\rho_{43} + i\frac{\Omega_{RF}}{2}(\rho_{44} - \rho_{33}) + i\frac{\Omega_c}{2}\rho_{42},
\end{aligned} \tag{12}$$

where  $\dot{\rho}_{ij}^* = \dot{\rho}_{ji}$  and \* represents the complex conjugate.

We numerically solve these equations to find the steady-state solution for  $\rho_{21}$  for various values of  $\Omega_c$ ,  $\Omega_p$ , and  $\Omega_{RF}$ . This is done by forming a matrix with the system of equations for  $\dot{\rho}_{ij} = 0$ . The null-space of this resulting system matrix is the steady-state solution. The steady-state solution for  $\rho_{21}$  is Doppler averaged in the usual way

$$\rho_{21D} = \frac{1}{\sqrt{\pi}u} \int_{-3u}^{3u} \rho_{21}(\Delta'_p, \Delta'_c) e^{-\frac{v^2}{u^2}} dv, \tag{13}$$

where  $u = \sqrt{2k_B T/m}$  and  $m$  is the mass of the atom. We use the case where the probe and coupling laser are counter-propagating. Thus, the frequency seen by the atom moving toward the probe beam is upshifted by  $2\pi v/\lambda_p$  (where  $v$  is the velocity of the atoms), while the coupling beam is downshifted by  $2\pi v/\lambda_c$ . Thus, the probe and coupling beam detunings are modified by the following:

$$\Delta'_p = \Delta_p - \frac{2\pi}{\lambda_p}v \quad \text{and} \quad \Delta'_c = \Delta_c + \frac{2\pi}{\lambda_c}v. \tag{14}$$

### III. NUMERICAL RESULTS FOR AT-SPLITTING

In this section, we investigate the AT-splitting (i.e.,  $\Delta f_o$ ) dependence on  $\Omega_c$  and  $\Omega_p$ . Figure 4 shows the EIT signal obtained from Eq. (3) for  $\Omega_{RF} = 2\pi \times (9.2 \text{ MHz})$  and different combinations of  $\Omega_p$  and  $\Omega_c$ . In our discussion, we use the combined quantity  $\Omega = \sqrt{\Omega_c^2 + \Omega_p^2}$ . The results are for  $T = 300 \text{ K}$  and for scanning the probe laser (indicated by  $\Delta_p$ ). Once the Doppler mismatch is taken into account, the separation between the two peaks for  $\Omega_{RF} = 2\pi \times (9.2 \text{ MHz})$  and probe detuning should be  $5.66 \text{ MHz}$  (i.e.,  $\Delta f_m = \Delta f_o \lambda_c / \lambda_p$ ,

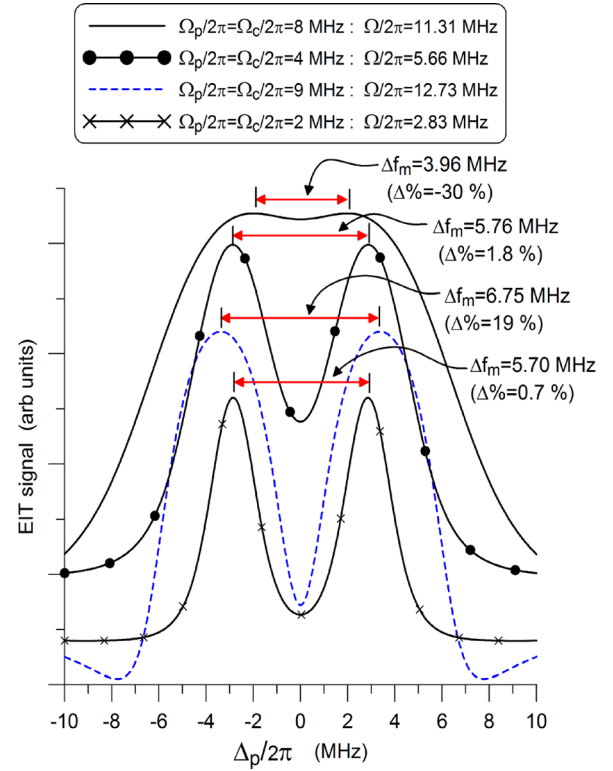


FIG. 4. Numerical data for the EIT signal (i.e., probe laser transmission through the cell) as a function of probe laser detuning  $\Delta_p$ . This dataset is for  $\Omega_{RF} = 2\pi \times (9.2 \text{ MHz})$  and for different values  $\Omega = \sqrt{\Omega_c^2 + \Omega_p^2}$  and with non resonant RF and coupling fields ( $\Delta_c = \Delta_{RF} = 0$ ).

where  $\Delta f_o = \Omega_{RF}$ , assuming the validity of the linear relationship). This figure shows that the AT-splitting (or  $\Delta f_o$ ) is not constant for a given value of  $\Omega_{RF}$  for the different values for  $\Omega$ . We see that the AT-splitting is either smaller or larger than  $\Omega_{RF}$  depending on the values of  $\Omega_p$  and  $\Omega_c$ . Recall that Eqs. (1) and (2) state that the AT-splitting should be constant for a given value of  $\Omega_{RF}$ . In the figure, we also indicate the percent difference between the measured splitting and  $\Omega_{RF}$  defined by

$$\Delta\% = 100 \times \frac{(2\pi \times \Delta f_o) - \Omega_{RF}}{\Omega_{RF}} \quad \text{and} \quad \Delta f_o = D \Delta f_m. \tag{15}$$

Notice that  $\Delta\%$  ranges from  $-30\%$  to  $19\%$  for the different values of  $\Omega$ , where a negative value indicates an underestimate and a positive value indicates an overestimate.

This non-linear behavior is further illustrated with the family of curves shown in Figs. 5(a) for  $\Omega_p = \Omega_c$ . The dashed reference line in this figure corresponds to  $\Delta f_o = \Omega_{RF}$ . For a given  $\Omega_c$  and  $\Omega_p$ , the linear behavior occurs only as  $\Omega_{RF}$  exceeds some minimum value. Below this value the curves become non-linear. The percentage difference ( $\Delta\%$ ) for these data is shown in Fig. 6(a). We see  $\Delta\%$  can be large in the non-linear region. Using  $\Delta f_o$  in these non-linear regions could result in large errors in the calculated E-field strength.

Figure 5(b) shows a set of curves for  $\Omega_p$  held fixed at  $2\pi \times (1.0 \text{ MHz})$  and various  $\Omega_c$ , and Fig. 5(c) shows a set of curves for  $\Omega_c$  held fixed at  $2\pi \times (1.0 \text{ MHz})$  and various  $\Omega_p$ .

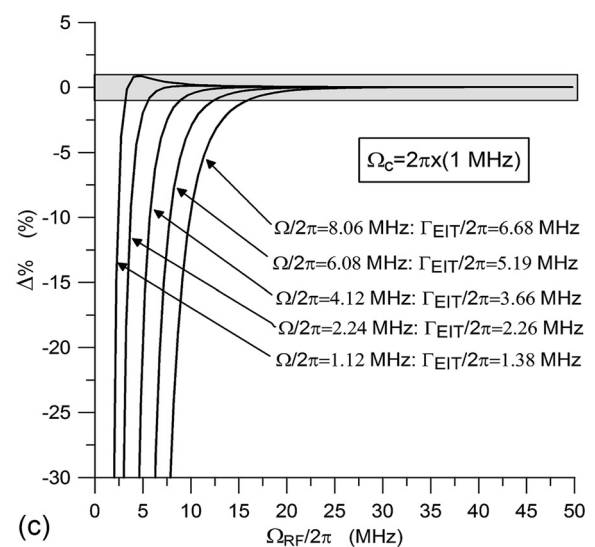
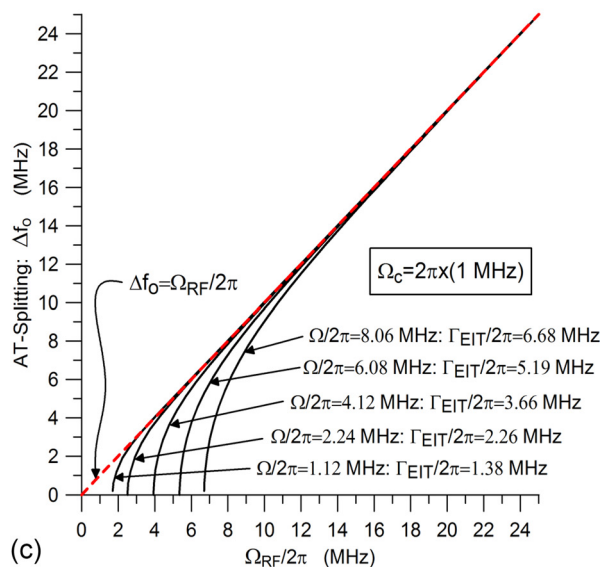
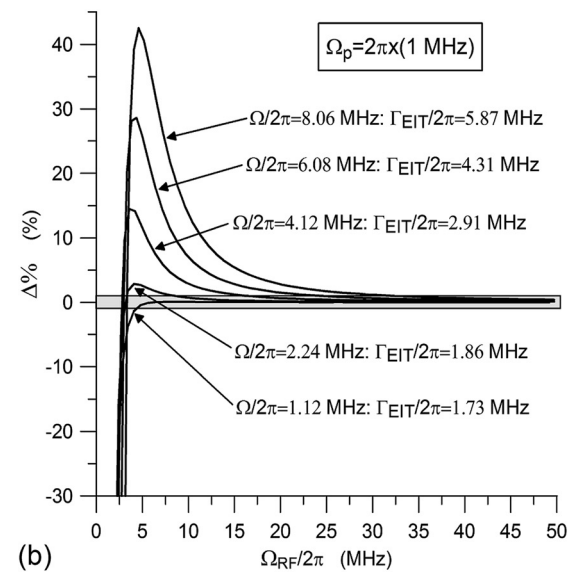
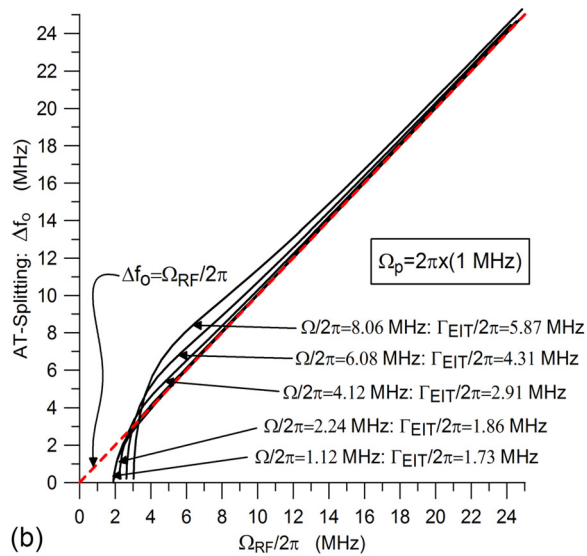
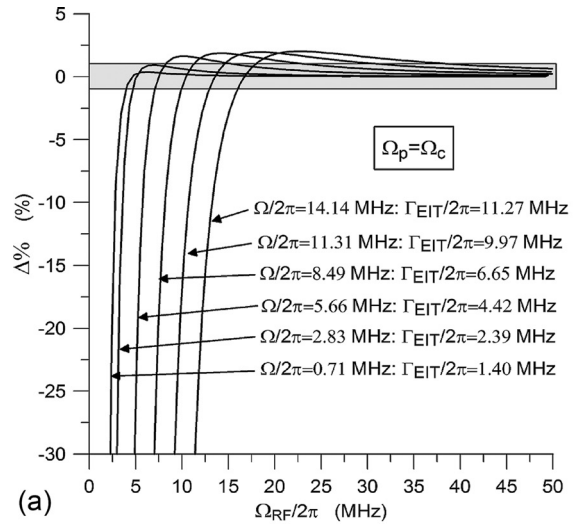
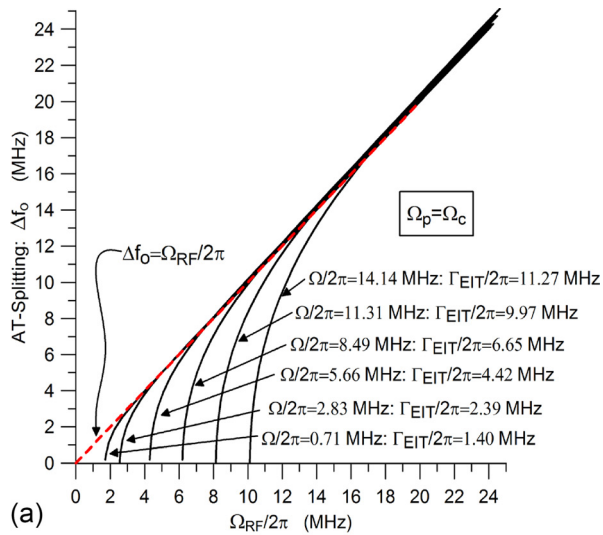


FIG. 5. Numerical calculations for  $\Delta f_0$  versus  $\Omega_{RF}/2\pi$  for  $T = 300 \text{ K}$ : (a)  $\Delta f_0$  versus  $\Omega_{RF}/2\pi$  for  $\Omega_p = \Omega_c$ . (b)  $\Delta f_0$  versus  $\Omega_{RF}/2\pi$  for  $\Omega_p = 2\pi \times (1.0 \text{ MHz})$ . (c)  $\Delta f_0$  versus  $\Omega_{RF}/2\pi$  for  $\Omega_c = 2\pi \times (1.0 \text{ MHz})$ .

FIG. 6. Numerical calculations for  $\Delta\%$  versus  $\Omega_{RF}/2\pi$  for  $T = 300 \text{ K}$ : The gray boxes in these curves indicate the region where  $|\Delta\%| < 1\%$ . (a)  $\Delta\%$  versus  $\Omega_{RF}/2\pi$  for  $\Omega_p = \Omega_c$ . (b)  $\Delta\%$  versus  $\Omega_{RF}/2\pi$  for  $\Omega_p = 2\pi \times (1.0 \text{ MHz})$ . (c)  $\Delta\%$  versus  $\Omega_{RF}/2\pi$  for  $\Omega_c = 2\pi \times (1.0 \text{ MHz})$ .

The percentage difference ( $\Delta\%$ ) for these data are shown in Figs. 6(b) and 6(c). The results in Fig. 5(b) [i.e., for  $\Omega_p = 2\pi \times (1.0 \text{ MHz})$ ] have an additional interesting feature in that the curves first overshoot the  $\Delta f_o = \Omega_{RF}$  reference line before dropping to  $\Delta f_o \approx 0$ . The overshoot increases with  $\Omega_c$ . The overshooting is caused by the enhanced absorption dips in the EIT signal. These enhanced absorption dips were first observed in Ref. 10 and are seen by the dashed curve in Fig. 4 at the  $\Delta_p = 2\pi \times (7.5 \text{ MHz})$  location. An enhanced absorption dip from one EIT line interferes with the peak of another EIT line, causing the peaks to be pushed further apart and resulting in a larger AT-splitting. As indicated in Fig. 6(b), the enhanced absorption dips cause much larger overestimates (i.e., positive  $\Delta\%$ ) when compared to the other cases [i.e., Figs. 6(a) and 6(c)].

The full-width half-maxima (FWHM) of the EIT linewidths ( $\Gamma_{EIT}$ ) for each curve are indicated in Figs. 5 and 6. (These values for  $\Gamma_{EIT}$  were obtained for  $\Omega_{RF} = 0$ .) We see that values for  $\Omega_{RF}$  where the non-linear behavior begins (i.e., the curves drop below the  $\Delta f_o = \Omega_{RF}$  line) decrease as  $\Gamma_{EIT}$  decreases (or as  $\Omega$  decreases). The highly non-linear behavior occurs when  $\Omega_{RF} \lesssim \Gamma_{EIT}$ . The AT peaks are artificially pulled closer together for simultaneously large  $\Gamma_{EIT}$  and small E-field values (or small  $\Delta f_o$ ). We see that for the cases in Fig. 5(c), as long as  $\Omega_{RF} \gtrsim 2\Gamma_{EIT}$ , the curves fall within the linear regions to within 1%. For the cases with enhanced absorption where there are large overshoots [see Fig. 5(b)], the curves are more complicated and  $\Omega_{RF}$  needs to be larger than  $3\Gamma_{EIT}$  to  $4\Gamma_{EIT}$  in order for the curves to start approaching the linear region to within 1%. These deviations from the linear behavior for all the cases in Fig. 5 result in a measurement uncertainty when determining the E-field strength with this EIT method. In Fig. 6, we have highlighted where these deviations are below 1%. This is indicated by the gray box region, which corresponds to  $|\Delta\%| < 1\%$ . For cases in Fig. 6(c), we see as long as  $\Omega_{RF} \gtrsim 2\Gamma_{EIT}$ , the deviation or the error in using Eq. (2) is less than 1% (i.e.,  $\Delta\% < 1\%$ ), and if  $\Omega_{RF} \gg 2\Gamma_{EIT}$  the deviation is decreased further to well below 0.5%. However, the cases in Figs. 6(b) and 6(a) are more problematic and can result in larger deviations. For the cases in Fig. 6(a),  $\Delta\% > 1\%$  unless  $\Omega_{RF} > 3\Gamma_{EIT}$ ; for the cases in Fig. 6(b),  $\Delta\% > 1\%$  unless  $\Omega_{RF}$  is larger than  $3\Gamma_{EIT}$  or  $4\Gamma_{EIT}$ . These results indicate that the most useful region to work within is shown in the cases in Fig. 6(c). An additional benefit of these cases is that they have the smallest value of  $\Omega_c$ . In fact, powers for the coupling laser to reach Rydberg states can be a critical experimental limitation, so working in regions where  $\Omega_c$  is small is convenient.

From the results in Fig. 5, it is seen that this non-linear behavior also leads to a critical value for  $\Omega_{RF}$  (defined as  $\Omega_{crit}$ ) before AT-splitting occurs. These critical values correspond to the minimum splitting that can be detected and is given by the locations where the curves touch the  $x$ -axis. The E-field cannot be measured with the AT-splitting method when  $\Omega_{RF} < \Omega_{crit}$ . No matter how small the value of  $\Omega$ , the value of  $\Omega_{RF}$ , where non-linear behavior begins, never approaches zero. This is due to the Doppler effect as a result of the temperature of the atomic vapor. The reason  $\Omega_{crit}$

never approaches zero can be seen in Fig. 7, where we show the calculated EIT linewidth versus  $\Omega$  for both our room temperature atomic vapor and a cold-atom scenario. We find that, as  $\Omega$  is reduced,  $\Gamma_{EIT}$  approaches a minimum value for the hot-atom case, whereas it reaches near-zero for cold atoms. The  $\Omega_{crit}$  has a lower limit of about 1.8 MHz for the hot-atom  $^{85}\text{Rb}$  case studies in this work. In Sec. IV, we explain how the temperature of the atomic vapor changes the measurement of an RF E-field by affecting the characteristics of the AT-splitting.

#### IV. HOT VERSUS COLD ATOMIC VAPOR

The region of the non-linear behavior is related to the temperature of the atomic vapor. From the results shown in Fig. 5, we see that as  $\Omega$  gets smaller, the location where the non-linear region starts is pulled to smaller values of  $\Omega_{RF}$ . However, at some point, no matter how small  $\Omega$  becomes, we cannot force the start of the non-linear region to zero. This is related to the Doppler effect of the room temperature atomic vapor and the natural linewidth of the probe transition. A question of interest is how vapor-cell (hot-atom) EIT emerges from the behavior of cold-atom EIT. In cold-atom EIT, there is no Doppler factor [i.e.,  $D = 1$  in Eq. (2)], and for small  $\Omega$ , the EIT linewidth follows  $\Gamma_{EIT} = (\Omega_c^2 + \Omega_p^2)/\Gamma_2$  (see Fig. 7). This allows, in principle, the measurement of very small RF-induced AT splittings, limited only by laser and Rydberg-level linewidths. The system gradually transitions from the cold- into the hot-atom case when the Doppler shifts in the sample become on the order of the linewidth of the probe transition. In the case of Rb Rydberg-EIT on the  $|5S_{1/2}\rangle \rightarrow |5P_{3/2}\rangle \rightarrow |Ryd\rangle$  cascade, the transition occurs between 1 mK and 1 K. In the hot-atom limit, the velocity averaging in Eq. (13) produces the Doppler factor in Eq. (2) and limits the EIT linewidth to

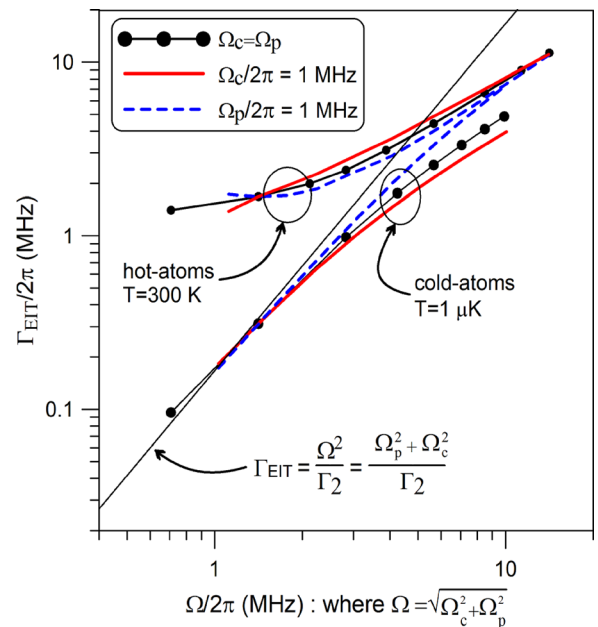


FIG. 7. Numerical data for  $\Gamma_{EIT}$  versus  $\Omega$ . We show results for both hot-atoms ( $T = 300 \text{ K}$ ) and cold-atoms ( $T = 1 \mu\text{K}$ ). These values were obtained for  $\Omega_{RF} = 0$ .

values above several MHz as shown in Fig. 7. This, in turn, limits the ability to measure RF fields via the AT-splitting method to fields with  $\Omega_{RF}$  larger than about 2 MHz, as evident in Fig. 5. Deviations from a linear relationship between the observed AT-splitting and  $\Omega_{RF}$ , as well as the loss in splitting contrast at low  $\Omega_{RF}$  and  $\Omega_c$  also follow from the velocity averaging.

Figure 8 explains the transition from cold- to hot-atom EIT by considering the absorption coefficient per velocity class [which is proportional to the integrand in Eq. (13)] as a function of atom velocity and the probe detuning  $\Delta_p$  for representative Rabi-frequency choices. In the cold-atom case (a), the velocity is practically zero, and the overall scattering profile is a Lorentzian with an FWHM of  $\Gamma_2$  along the  $\Delta_p$ -axis. With a small laser linewidth, the Rydberg-EIT linewidth,  $\Gamma_{EIT} = (\Omega_c^2 + \Omega_p^2)/\Gamma_2$ , can be made very narrow; in Fig. 8(a)  $\Gamma_{EIT} = 2\pi \times 300$  kHz. According to Section II, at a fixed velocity, the AT-splitting is given by  $\Omega_{RF}$ . The observable EIT spectrum follows from the integral along the velocity axis in Fig. 8(a), leading to two narrow EIT dips within a  $2\pi \times 6$  MHz wide Lorentzian. It is thus seen that at low

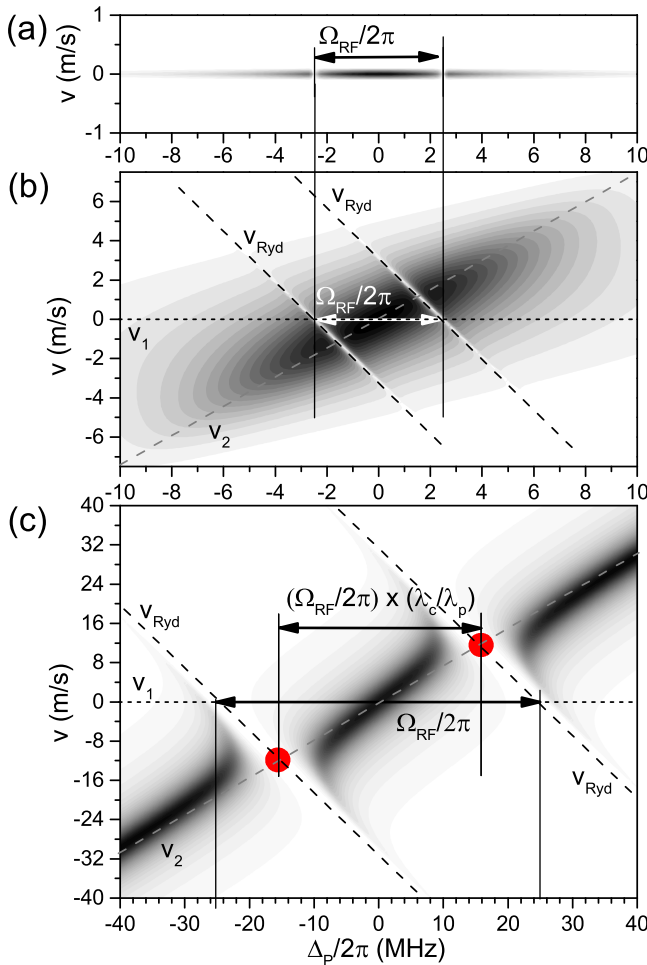


FIG. 8. Calculated absorption per velocity, in arb. un., vs atom velocity and probe detuning  $\Delta_p$ : (a) in a cold-atom case with  $T = 10 \mu\text{K}$ ,  $\Omega_p/(2\pi) = 1$  MHz,  $\Omega_c/(2\pi) = 1$  MHz and  $\Omega_{RF}/(2\pi) = 5$  MHz, (b) in a cold-atom case with  $T = 10 \text{ mK}$  and with the same parameters as in case (a), and (c) in a hot-atom (vapor-cell) case with  $T = 300 \text{ K}$ ,  $\Omega_p/(2\pi) = 5$  MHz,  $\Omega_c/(2\pi) = 20$  MHz, and  $\Omega_{RF}/(2\pi) = 50$  MHz. The dashed lines in (b) and (c) show the functions in Eq. (16).

temperature, atom-based RF electric-field measurement via determination of AT splittings in EIT spectra, and using Eq. (2) with a Doppler factor  $D = 1$ , can be performed down to very small values of  $\Omega_{RF}$ . While there is a lower limit set by laser linewidth, interaction time, level dephasing, etc., lower limits for  $\Omega_{RF}$  in the range  $\leq 100$  kHz seem quite feasible. For a (typical) transition dipole moment of  $1000 e a_0$  (where  $e$  is the elementary charge and  $a_0$  is the Bohr radius), this translates into an RF-field sensitivity in the range of  $\leq 10$  mV/m. When scanning the probe laser, there is an upper limit to the strongest RF fields that can be measured; here, the cold-atom Rydberg-EIT-AT method requires  $\Omega_{RF} \lesssim 2\pi \times 10$  MHz, due to the finite probe-transition linewidth  $\Gamma_2$ . This results in an upper limit for the RF field that can be measured. However, that limitation can be easily eliminated by scanning the coupler-laser detuning,  $\Delta_c$ , and using a fixed  $\Delta_p = 0$ .

Atom-based RF electric-field measurement via determination of AT splittings in cold-atom EIT spectra benefits from the absence of significant Doppler effects. A typical case of hot-atom EIT is shown in Fig. 8(c). The dressed-atom energy levels that arise from Eq. (14) correspond to the following lines in the velocity vs  $\Delta_p$  map:

$$\text{Ground state : } v_1(\Delta_p) = 0$$

$$\text{Intermediate state : } v_2(\Delta_p) = \frac{\lambda_p \Delta_p}{2\pi}$$

$$\text{AT-split Rydberg pairs : } v_{Ryd}(\Delta_p) = \frac{1}{2\pi} \left( \Delta_p \pm \frac{\Omega_{RF}}{2} \right) \frac{\lambda_p \lambda_c}{\lambda_p - \lambda_c}. \quad (16)$$

The lines for ground and Rydberg states are largely hidden in the plots in Figs. 8(b) and 8(c) because those levels do not scatter photons, except near the dressed-state avoided crossings. The coupler field leads to avoided crossings between intermediate and Rydberg states; in the vicinity of the crossings, the intermediate-state character is partially shared with the Rydberg levels, making them “visible” in the absorption map. At fixed velocity, the AT-split Rydberg levels are still separated by  $\Omega_{RF}$  (same as in the cold-atom case). Also, away from the crossings, the width of the absorption profile associated with the intermediate level is  $\Gamma_2$ .

The measurable EIT spectrum arises from the velocity integral of the results given in Fig. 8. The observed splitting between the EIT-AT dips is given by the separation of the projections of the red dots in Fig. 8(c) onto the  $x$ -axis. Straightforward analysis leads to Eq. (2) with the Doppler factor  $D$ . It also becomes obvious that the velocity integration leads to a minimum observable  $\Omega_{RF}$  that is given by  $\Gamma_2$ ,  $\Omega_c$ , and  $\Omega_p$ . Basically,  $\Omega_c$  cannot be reduced to arbitrarily small values without losing the EIT absorption dips after performing the velocity integral. This is visualized in Fig. 8(b), where  $\Gamma_{EIT}$  is so low that the EIT signatures get lost in the velocity averaging process. The lowest  $\Omega_c$  at which the EIT lines can still be observed scales with  $\Gamma_2$ . This, in turn, sets a lower limit of  $\Omega_{RF}$  below which the RF field will not cause an AT splitting of the EIT line. From Eq. (16), it is further

noted that in a Doppler matched case (i.e.,  $\lambda_p = \lambda_c$ ), the velocities of the Rydberg dressed states versus  $\Delta_p$  in Fig. 8 would be vertical lines. In this case, the EIT features would not get washed out in the velocity averaging process. Hence, the lower limit of  $\Omega_{RF}$  can be avoided by selecting a Doppler-matched case.

The EIT spectra in Fig. 9 show the Beer's absorption coefficient [as defined in Eq. (3)] in a Rb sample of fixed density for a range of temperatures. The top four traces all use the same combination of  $\Omega_p/2\pi = \Omega_c/2\pi = 1$  MHz and  $\Omega_{RF}/2\pi = 5$  MHz. For traces 1, 2, 3, 4, the temperature is varied from  $T = 10 \mu\text{K}$ , 1 mK, 0.1 K, to 10 K, and the measured AT-splitting for each is 5.0 MHz, 4.8 MHz, 3.8 MHz, and 3.1 MHz. At 10  $\mu\text{K}$ , the measured AT-splitting is equal to the incident  $\Omega_{RF}$ , for a Doppler factor of  $D = 1$ , while beyond 10 K the measured AT-splitting is a fraction of  $\Omega_{RF}$ , leading to the Doppler correction of  $D = \lambda_p/\lambda_c$  as in Eq. (2). Trace 5 shows that this factor remains as  $\Omega_p$ ,  $\Omega_c$ , and  $\Omega_{RF}$  are varied, and trace 6 shows that  $D$  does not change as the temperature is increased from 10 K to 300 K.

Another feature that can be seen in Fig. 9 is that the visibility of the AT-splitting varies with  $\Omega$ . As  $\Omega$  is reduced, both the minimum observable RF Rabi frequency  $\Omega_{crit}$  and the visibility of the AT-splitting are reduced. This introduces another trade-off for measuring a weak RF E-field. As  $\Omega$  is lowered to detect a smaller minimum  $\Omega_{RF}$ , the ability to resolve the AT-splitting is also reduced. The visibility  $V$  for a range of values of  $\Omega$  is plotted in Fig. 10. Here we define visibility as  $V = (\alpha_{max} - \alpha_{min})/\alpha_{max}$ , where  $\alpha_{min}$  and  $\alpha_{max}$  are the minimum absorption coefficients at the bottom of the EIT dips and the maximum coefficient in between the two dips, respectively. For Rb, requiring a splitting visibility  $V \geq 0.1$  leads to a lowest value of  $\Omega_{RF}$  that can be measured on the order of 3 MHz. This limit applies to RF E-field

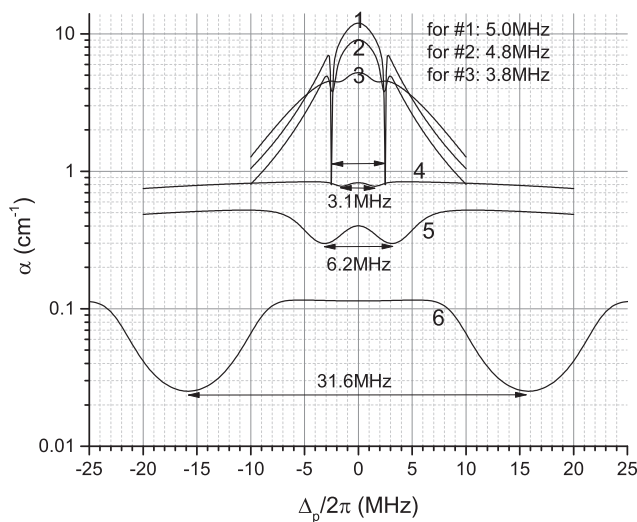


FIG. 9. Calculated EIT spectra vs. probe detuning for a range of temperatures. To show the effect of temperature on the probe absorption coefficient,  $\alpha$ , the atom density is held fixed at  $7.3 \times 10^9 \text{ cm}^{-3}$ . The parameters  $T$ ,  $\Omega_p/(2\pi)$ ,  $\Omega_c/(2\pi)$ , and  $\Omega_{RF}/(2\pi)$  are, for the plots labeled 1–6, (1) 10  $\mu\text{K}$ , 1, 1, and 5 MHz; (2) 1 mK, 1, 1, and 5 MHz; (3) 0.1 K, 1, 1, and 5 MHz; (4) 10 K, 1, 1, and 5 MHz; (5) 10 K, 5, 5, and 10 MHz; and (6) 300 K, 5, 20, and 50 MHz. The frequencies of the AT-splitting for each case are indicated on the figure.

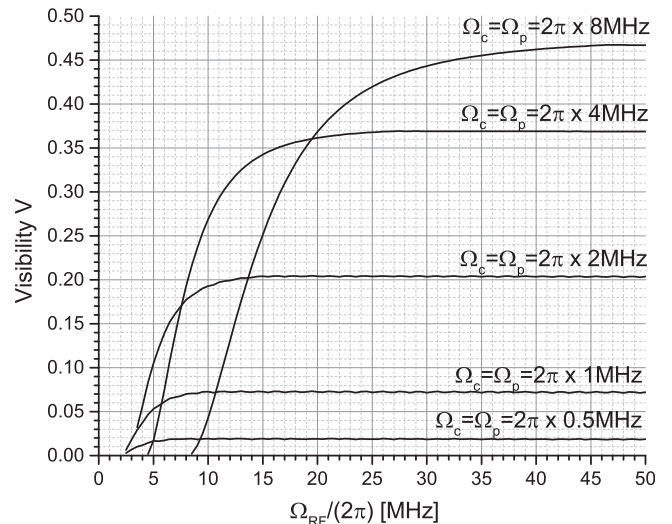


FIG. 10. Visibility  $V$  of the Rydberg-EIT-AT splitting, as defined in the text, vs RF Rabi frequency  $\Omega_{RF}$  for the indicated values of  $\Omega_p$  and  $\Omega_c$  in a 300-K vapor cell. It is seen that high coupler Rabi frequencies lead to better visibility of the AT-split EIT lines at high  $\Omega_{RF}$ , but greatly reduce the applicability of the Rydberg-EIT-AT splitting method at low  $\Omega_{RF}$ .

measurements via the Rydberg-EIT-AT splitting method in hot vapor cells, which is the most common and robust method for the atom-based RF field measurement. Lower limits can be achieved in less robust methods, such as cold-atom EIT, a detailed signal analysis of Rydberg-EIT lines in RF fields that are too weak to split the EIT line into a resolved AT pair,<sup>3</sup> or a 3-photon EIT method.<sup>20,21</sup>

As an atomic vapor transitions from the cold- to the hot-atom case, the Doppler factor  $D$  in Eq. (2) changes from  $D = 1$  to  $D = \lambda_p/\lambda_c$ ; for Rb, this transition occurs between 100  $\mu\text{K}$  and 1 K. For small values of  $\Omega$ , the EIT linewidth scaling with the pump and probe Rabi frequencies changes from  $\Gamma_{EIT} = (\Omega_p^2 + \Omega_c^2)/\Gamma_2$  to a more complicated relationship that has a lower limit for  $\Gamma_{EIT}$  of  $\sim 1.5$  MHz (as shown in Fig. 7). Consequently, there is a minimum RF Rabi frequency ( $\Omega_{crit}$ ) above which an AT-splitting in the hot-atom case can be observed. The visibility of the AT-splitting is likewise affected, setting an effective minimum resolvable  $\Omega_{RF}$  for this particular method.

## V. CONCLUSION/DISCUSSION

We explored the conditions under which the linear relationship between the measured Autler-Townes splitting ( $\Delta f_o$ ) and the RF Rabi frequency ( $\Omega_{RF}$ ) is valid. This is key to assessing the uncertainty of this measurement approach. We show that the linear relationship of these two quantities is valid as long as  $\Omega_{RF}$  is greater than twice the EIT linewidth ( $2\Gamma_{EIT}$ ). In this region, we determined that the error in the assumed linear relationship can be limited to  $<1\%$ , and if  $\Omega_{RF} \gg 2\Gamma_{EIT}$ , the deviation is decreased further to well below 1%. While the AT split is resolvable when the RF Rabi frequency is below  $2\Gamma_{EIT}$ , the pump and probe Rabi frequencies can no longer be neglected, causing the relationship between  $\Delta f_o$  and  $\Omega_{RF}$  to become non-linear. The non-linear behavior also leads to a critical value for  $\Omega_{RF}$ , which corresponds to the minimum splitting that can be detected, and as

a result, an E-field cannot be measured with the AT-splitting method when  $\Omega_{RF} < \Omega_{crit}$ . If we used the linear relationship [i.e., Eq. (2)] to estimate the E-field strength when  $\Omega_{RF}$  approaches  $\Omega_{crit}$ , the uncertainties in the field strength measurements can be very large (over 30% to 50%). With the knowledge of the probe and coupling Rabi frequencies, the relationship between  $\Delta f_o$  and  $\Omega_{RF}$  can, in principle, be calculated with the model presented here, reducing the measurement uncertainty when  $\Omega_{RF}$  is below the  $2\Gamma_{EIT}$  limit, but a closed-form expression cannot be used (because it is not available for these cases).

Another strategy to reduce this limit is to reduce the EIT linewidth. We find that reducing the probe and coupling Rabi frequencies reduces the EIT linewidth only to a minimum that is limited by the Doppler broadening. To reduce this further requires lowering the temperature of the atomic vapor. In our discussion of the effect of temperature on the relationship between  $\Delta f_o$  and  $\Omega_{RF}$ , we show that the dependence of  $\Gamma_{EIT}$  on  $\Omega_p$  and  $\Omega_c$  is different above and below a temperature threshold. Below this threshold,  $\Gamma_{EIT}$  can be made arbitrarily small, allowing measurements of very weak  $\Omega_{RF}$ . Above this threshold, there is a lower limit on  $\Gamma_{EIT}$ , which limits the range in which the relationship between  $\Delta f_o$  and  $\Omega_{RF}$  is linear.

Finally, the 3-photon scheme discussed in Ref. 20 allows, in principle, for narrower EIT linewidths ( $\Gamma_{EIT}$ ) in vapor-cell Rydberg EIT and for measurements of weaker E-field strengths (i.e., smaller  $\Omega_{RF}$ ). The technique in Ref. 20 is based on a coincidental wavelength combination and has shown theoretically to produce linewidths of about 10 kHz. To observe a kHz linewidth, one must decrease the power to avoid power broadening. This will increase the shot noise, reducing the sensitivity.<sup>20,21</sup> The technique has not been realized experimentally as of yet, but does show promise.

## ACKNOWLEDGMENTS

This work was partially supported by the Defense Advanced Research Projects Agency (DARPA) under the QuASAR Program and by NIST through the Embedded Standards program, as well as by the NSF (PHY-1506093) and Rydberg Technologies, LLC. We thank Dr. J. P. Shaffer

from The University of Oklahoma for his useful technical discussions on 3-photon Rydberg excitation.

- <sup>1</sup>C. L. Holloway, M. T. Simons, J. A. Gordon, P. F. Wilson, C. M. Cooke, D. A. Anderson, and G. Raithel, *IEEE Trans. Electromagn. Compat.* **59**(2), 717–728 (2017).
- <sup>2</sup>C. L. Holloway, J. A. Gordon, A. Schwarzkopf, D. A. Anderson, S. A. Miller, N. Thaicharoen, and G. Raithel, *IEEE Trans. Antenna Propag.* **62**(12), 6169–6182 (2014).
- <sup>3</sup>J. A. Sedlacek, A. Schwettmann, H. Kübler, R. Löw, T. Pfau, and J. P. Shaffer, *Nat. Phys.* **8**, 819 (2012).
- <sup>4</sup>C. L. Holloway, J. A. Gordon, A. Schwarzkopf, D. A. Anderson, S. A. Miller, N. Thaicharoen, and G. Raithel, *Appl. Phys. Lett.* **104**, 244102 (2014).
- <sup>5</sup>J. A. Gordon, C. L. Holloway, A. Schwarzkopf, D. A. Anderson, S. A. Miller, N. Thaicharoen, and G. Raithel, *Appl. Phys. Lett.* **105**, 024104 (2014).
- <sup>6</sup>J. A. Sedlacek, A. Schwettmann, H. Kübler, and J. P. Shaffer, *Phys. Rev. Lett.* **111**, 063001 (2013).
- <sup>7</sup>H. Fan, S. Kumar, J. Sedlacek, H. Kübler, S. Karimkashi, and J. P. Shaffer, *J. Phys. B: At. Mol. Opt. Phys.* **48**, 202001 (2015).
- <sup>8</sup>M. Tanasittikosol, J. D. Pritchard, D. Maxwell, A. Gauguet, K. J. Weatherill, R. M. Potvliege, and C. S. Adams, *J. Phys. B* **44**, 184020 (2011).
- <sup>9</sup>C. G. Wade, N. Sibalic, N. R. de Melo, J. M. Kondo, C. S. Adams, and K. J. Weatherill, *Nat. Photonics* **11**, 40–43 (2017).
- <sup>10</sup>A. K. Mohapatra, T. R. Jackson, and C. S. Adams, *Phys. Rev. Lett.* **98**, 113003 (2007).
- <sup>11</sup>M. T. Simons, J. A. Gordon, and C. L. Holloway, *J. Appl. Phys.* **120**, 123103 (2016).
- <sup>12</sup>D. A. Steck, see <http://steck.us/alkalidata> for Rubidium 85 D line data (revision 2.1.6, 20 September 2013).
- <sup>13</sup>P. R. Berman and V. S. Malinovsky, *Principles of Laser Spectroscopy and Quantum Optics* (Princeton University Press, 2011).
- <sup>14</sup>C. L. Holloway, J. A. Gordon, M. T. Simons, H. Fan, S. Kumar, J. P. Shaffer, D. A. Anderson, A. Schwarzkopf, S. A. Miller, N. Thaicharoen, and G. Raithel, in *EMC 2015: Joint IEEE International Symposium on Electromagnetic Compatibility and EMC Europe, Dresden, Germany, August 16–22, 2015*, pp. 467–472.
- <sup>15</sup>H. Fan, S. Kumar, J. Sheng, J. P. Shaffer, C. L. Holloway, and J. A. Gordon, *Phys. Rev. Appl.* **4**, 044015 (2015).
- <sup>16</sup>H. Zhang, L. Zhang, L. Wang, S. Bao, J. Zhao, and G. Raithel, *Phys. Rev. A* **90**, 043849 (2014).
- <sup>17</sup>P. M. Anisimov, J. P. Dowling, and B. C. Sanders, *Phys. Rev. Lett.* **107**, 163604 (2011).
- <sup>18</sup>T. Y. Abi-Salloum, *J. Mod. Opt.* **57**(14), 1366–1376 (2010).
- <sup>19</sup>M. T. Simons, J. A. Gordon, C. L. Holloway, D. A. Anderson, S. A. Miller, and G. Raithel, *Appl. Phys. Lett.* **108**, 174101 (2016).
- <sup>20</sup>S. Kumar, H. Fan, J. Sheng, and J. P. Shaffer, *Sci. Rep.* **7**, 42981 (2017).
- <sup>21</sup>S. Kumar, H. Fan, H. Kübler, A. Jozani, and J. P. Shaffer, *Opt. Express* **25**, 8625 (2017).